Numerical Homogenization of 2D Heterogeneous Anisotropic Porous Medium Based on a Hyperbolic Thermodynamically Compatible Model

Galina Reshetova[1] and Evgeniy Romenski[2(✉)]

[1] Trofimuk Institute of Petroleum Geology and Geophysics SB RAS, Novosibirsk 630090, Russia
kgv@nmsf.sscc.ru

[2] Sobolev Institute of Mathematics SB RAS, Novosibirsk 630090, Russia
evrom@math.nsc.ru

Abstract. For the numerical homogenization of a heterogeneous porous medium, a method based on strain energy is proposed in combination with a hyperbolic thermodynamically compatible model of a saturated porous medium. The solution of stationary equilibrium problems, necessary for calculating the effective compliance moduli by comparing the energy of an inhomogeneous medium with the equivalent elastic energy, is obtained by the time-marching to a stationary solution method. A number of numerical examples for calculating the effective moduli of macroscopically anisotropic heterogeneous porous samples are presented and discussed.

Keywords: Numerical homogenization · Fluid saturated porous medium · Effective elastic moduli · Hyperbolic thermodynamically compatible model · Staggered grid finite difference scheme

1 Introduction

The evaluation of effective elastic moduli of heterogeneous media is of interest in many applied engineering sciences, for example, in seismic exploration, the development of new materials with specified properties, biomechanics, 3D printing and so on.

There are a number of methods for evaluating the effective moduli of heterogeneous media, a far from complete list of which includes: asymptotic homogenization for periodic structures based on the analytical method of decomposition of fields in terms of a small parameter (the ratio of the microstructure scale to the macroscale), see [16] and references therein; the classical method of representative volume element, in which for a minimum volume of material containing all statistical features of the microstructure, the stiffness tensor is calculated by averaging the stress and strain fields over the volume [1,4,6,17]; the FFT-based

© The Author(s), under exclusive license to Springer Nature Switzerland AG 2027
O. Gervasi et al. (Eds.): ICCSA 2026 Workshops, LNCS 16761, pp. 84–97, 2027.
https://doi.org/10.1007/978-3-032-30527-5_6

homogenization method, in which the solution of the equilibrium equations is sought in the frequency domain using the fast Fourier transform [2,15]; variational homogenization methods which uses variational principles to obtain strict upper and lower bounds on the effective properties of materials (see [5,7,20] and references therein.

We propose a novel numerical homogenization method using a strain energy-based approach [3,14,18,19], which essentially calculates the strain energy of an inhomogeneous medium and compares it with the energy of an equivalent elastic medium. This allows us to calculate all components of the compliance tensor by solving a series of simple equilibrium problems for stressed samples. We apply a strain energy-based method to a linear Hyperbolic Thermodynamically Compatible (HTC) model of porous media, which allows simulating wave processes in porous media with inclusions of pure solid and fluid phases using a single system of partial differential equations by a diffuse interphase approach. The linear HTC equations we use is derived from the general model [13] of a saturated porous medium for the case of finite deformations. It can be generalized to the case where the saturating fluid is a mixture of several fluids [12], and some applications of it can be found in the papers [8–10]. The governing equations of the model belong to the class of hyperbolic thermodynamically compatible systems, which ensures their solvability and allows the use of effective numerical methods. To solve a series of stationary problems required for the application of the strain energy-based method, we apply the time-marching method in conjunction with a finite difference scheme on staggered grids to obtain the equilibrium solution.

The rest of the paper is organized as follows. In Sect. 2 the governing equations of HTC linear poroelasticity are formulated. In Sect. 3 the strain energy-based method and test problems required for calculation of compliance moduli are presented. Section 4 briefly describes the time marching method applied for solving test problems studied in the next Sect. 5. This section presents the simulation results for various samples of porous media with differently oriented inclusions having other properties. In this section, the obtained anisotropy properties of the samples under consideration are also discussed.

2 Governing Equations of the Fluid Saturated Porous Medium in Case of Small Deformations

The numerical homogenization method presented in the paper is based on the use of a Hyperbolic Thermodynamically Compatible (HTC) model of fluid saturated porous media to calculate the strain energy of a heterogeneous porous sample in a stressed equilibrium state and its subsequent comparison with the strain energy of an equivalent elastic sample. Such a comparison allows us to compute the effective compliance moduli and then the stiffness moduli and sound velocities.

To calculate the deformation energy of a saturated porous medium, a linear system of equations is used, obtained by linearization the equations of the full HTC model of a two-phase solid-fluid medium [13]. Linearization is carried out for the solution of the complete system in a steady, stress-free state with a given

phase volume fractions of saturating fluid and skeleton α_1, α_2 ($\alpha_1 + \alpha_2 = 1$) and mass densities ρ_1, ρ_2.

It is assumed that in the three-dimensional space x_1, x_2, x_3, the porous medium, considered as a two-phase mixture, is characterized by the following state variables.:

- u_i, $(i = 1, 2, 3)$ - the velocity of the mixture along the axes x_i.
- w_i, $(i = 1, 2, 3)$ - the relative velocity of movement of the first phase relative to the second phase.
- p - the pressure in the medium.
- $\Sigma_{ij} = \Sigma_{ji}$ $(i, j = 1, 2, 3)$ - the stress deviator ($\Sigma_{11} + \Sigma_{22} + \Sigma_{33} = 0$).

It should be noted that the linear system is derived under the assumption of pressure equilibrium, that is, it is assumed that the pressures of the fluid and the solid skeleton are equal.

The complete system of governing equations reads as

$$\rho \frac{\partial u_i}{\partial t} + \frac{\partial p}{\partial x_i} - \frac{\partial \Sigma_{ik}}{\partial x_k} = 0, \tag{1a}$$

$$\frac{\partial w_i}{\partial t} + \left(\frac{1}{\rho_1} - \frac{1}{\rho_2}\right) \frac{\partial p}{\partial x_i} = -\lambda w_i, \tag{1b}$$

$$\frac{\partial p}{\partial t} + K \frac{\partial u_k}{\partial x_k} + \frac{\alpha_1 \alpha_2}{\rho} (\rho_2 - \rho_1) K \frac{\partial w_k}{\partial x_k} = 0, \tag{1c}$$

$$\frac{\partial \Sigma_{ik}}{\partial t} - \mu \left(\left(\frac{\partial u_i}{\partial x_k} + \frac{\partial u_k}{\partial x_i} \right) - \frac{2}{3} \delta_{ik} \left(\frac{\partial u_1}{\partial x_1} + \frac{\partial u_2}{\partial x_2} + \frac{\partial u_3}{\partial x_3} \right) \right) = -\frac{\Sigma_{ik}}{\tau}, \tag{1d}$$

and consists of the total momentum Eq. (1a), equation for the relative velocity (1b), equation for the pressure (1c) and equation for the stress deviator (1d).

Here $i, k = 1, 2, 3$ are the spacial indices, $\rho = \alpha_1 \rho_1 + \alpha_2 \rho_2$ is the mixture density. $K = \left(\frac{\alpha_1}{K_1} + \frac{\alpha_2}{K_2} \right)^{-1}$ is the bulk modulus of the two-phase mixture, where K_1, K_2 are the bulk moduli of the phases. $\mu = \rho V_s^2 = \rho(c_1 V_{s1}^2 + c_2 V_{s2}^2) = \alpha_1 \mu_1 + \alpha_2 \mu_2$ is the shear modulus of the mixture, $V_{sa} (a = 1, 2)$ are the phase shear velocities, $\mu_a = \rho_a V_{sa}^2 (a = 1, 2)$ are the phase shear moduli. If one of the phases, for example the first, is a liquid, we assume that its shear modulus is zero, and hence $\mu = \alpha_2 \mu_2$. Throughout the paper the repeating indices denote the summation over the corresponding index.

There are two dissipative sources in the system (1): $-\lambda w_i$ describes interfacial friction with the relaxation rate of the relative velocity λ, and $-\frac{\Sigma_{ik}}{\tau}$ describes the relaxation of the shear stress. In our studies, we neglect these terms, since our goal is to derive effective elastic moduli for reversible processes.

The stress deviator Σ_{ik} and pressure P are connected with the Almansi strain tensor ε_{ij} via linear relationships

$$\Sigma_{ik} = 2\mu \left(\varepsilon_{ik} - \delta_{ik} \frac{(\varepsilon_{11} + \varepsilon_{22} + \varepsilon_{33})}{3} \right), \quad P = -K(\varepsilon_{11} + \varepsilon_{22} + \varepsilon_{33}). \tag{2}$$

with defined above bulk and shear moduli $K = \left(\frac{\alpha_1}{K_1} + \frac{\alpha_2}{K_2}\right)^{-1}$, $\mu = \alpha_1\mu_1 + \alpha_2\mu_2$. These relations are used to derive the (1) system from the general HTC system of a saturated porous medium [13]. It should be noted that, if necessary, the Lamé constant λ can be calculated from the definition of the bulk modulus $K = \lambda + \frac{2}{3}\mu$ if the Lamé constant μ (shear modulus) is known. The total stress tensor of the saturated porous medium can be computed as $\sigma_{ik} = \Sigma_{ik} - P\delta_{ij}$ and is connected to the Almansi strain tensor ε_{ik} via Hooke's law for isotropic linear elasticity:

$$\sigma_{ik} = \lambda(\varepsilon_{11} + \varepsilon_{22} + \varepsilon_{33})\delta_{ik} + 2\mu\varepsilon_{ik}. \tag{3}$$

A very important property of the presented model of a porous medium, which we will need later to calculate the effective moduli, is the presence of an additional law of conservation of energy. The total energy for the solution to system (1) can be defined as $\mathcal{E} = \mathcal{E}_1 + \mathcal{E}_2$, where

$$\mathcal{E}_1 = \rho\frac{u_k u_k}{2} + \rho c_1 c_2 \frac{w_k w_k}{2},\ \mathcal{E}_2 = \frac{p^2}{2K} + \frac{\Sigma_{ij}\Sigma_{ji}}{4\mu}. \tag{4}$$

Assuming no dissipation and using the definition of (4), the law of conservation of energy follows from Eq. (1) and reads as

$$\frac{\partial \mathcal{E}}{\partial t} + \frac{\partial \Pi_k}{\partial x_k} = -\mathcal{Q}, \tag{5}$$

where $\Pi_k = u_k P + \frac{\alpha_1\alpha_2}{\rho}(\rho_2 - \rho_1)w_k P - u_i\Sigma_{ik}$ is the energy flux.

We emphasize that the two-phase model formulated in this section for a non-zero shear modulus of the first phase ($\mu_1 \neq 0$) can describe wave processes in a solid-solid mixture.

As described below, the strain energy-based numerical homogenization method involves calculating the energy $\mathcal{E}_2$ for a number of simple equilibrium problems and comparing it with the energy of an equivalent elastic medium.

3 Strain Energy of Homogeneous Elastic Medium. Calculation of Compliance Moduli by Solving Simple Equilibrium Problems

The stress-strain relations for an arbitrary linear-elastic medium can be written in two equivalent forms of Hooke's law:

$$\sigma_{ij} = c_{ijkl}\varepsilon_{kl}, \tag{6}$$

$$\varepsilon_{ij} = s_{ijkl}\sigma_{kl}, \tag{7}$$

where c_{ijkl} is the stiffness tensor and s_{ijkl} is the compliance tensor, which is inverse to the stiffness tensor.

The elastic energy expressed through the strain tensor has the following form

$$\mathcal{U} = \frac{1}{2}\sigma_{ij}\varepsilon_{ij} = \frac{1}{2}c_{ijkl}\varepsilon_{kl}\varepsilon_{ij}, \tag{8}$$

and can be written in equivalent form in terms of stress tensor

$$\mathcal{U} = \frac{1}{2}\sigma_{ij}\varepsilon_{ij} = \frac{1}{2}s_{ijkl}\sigma_{kl}\sigma_{ij}. \tag{9}$$

The latter formula (9) gives a direct way to calculate the components of the compliance tensor by solving a set of simple equilibrium problems.

Below we study the two-dimensional case of plane strain, for which $\varepsilon_{33} = \varepsilon_{13} = \varepsilon_{23} = \varepsilon_{31} = \varepsilon_{32} = 0$ and elastic energy (9) is equal to

$$\begin{aligned}\mathcal{U} = &\frac{1}{2}\left(\sigma_{11}\varepsilon_{11} + 2\sigma_{12}\varepsilon_{12} + \sigma_{22}\varepsilon_{22}\right) = \\ &s_{1111}(\sigma_{11})^2 + 2s_{1122}\sigma_{11}\sigma_{22} + s_{2222}(\sigma_{22})^2 + \\ &2s_{1212}\sigma_{12}\sigma_{12} + 2s_{1112}\sigma_{11}\sigma_{12} + 2s_{2212}\sigma_{22}\sigma_{12}.\end{aligned} \tag{10}$$

Let us consider two-dimensional elasticity equilibrium equations

$$\frac{\partial \sigma_{ij}}{\partial x_j} = 0, \quad i,j = 1,2. \tag{11}$$

in a rectangle $[-L_x, L_x] \times [-L_y, L_y]$ of volume $V = 2L_x \times 2L_y$.

To determine the six components of the compliance tensor s_{1111}, s_{1122}, s_{2222}, s_{1212}, s_{1112}, s_{2212} we need to solve six equilibrium boundary problems for Eq. (11) in the two-dimensional domain $[-L_x, L_x] \times [-L_y, L_y]$:

- Test 1
  $\sigma_{11}|_{x=\pm L_x} = 1, \quad \sigma_{22}|_{y=\pm L_y} = 0, \quad \sigma_{12}|_{x=\pm L_x} = 0, \quad \sigma_{12}|_{y=\pm L_y} = 0.$
  In this test problem, the deformation energy $\mathcal{U}^0$ is calculated, and at equilibrium it is equal to $\mathcal{U}^{01} = \frac{V}{2}s_{1111}(\sigma_{11})^2 = \frac{V}{2}s_{1111}$. Using this energy value, we find the compliance modulus s_{1111}.
- Test 2
  $\sigma_{11}|_{x=\pm L_x} = 0, \quad \sigma_{22}|_{y=\pm L_y} = 1, \quad \sigma_{12}|_{x=\pm L_x} = 0, \quad \sigma_{12}|_{y=\pm L_y} = 0.$
  And in this test problem we find the energy $\mathcal{U}^0$. For the equilibrium solution it is equal to $\mathcal{U}^{02} = \frac{V}{2}s_{2222}(\sigma_{22})^2 = \frac{V}{2}s_{2222}$, and therefore we find s_{2222}.
- Test 3
  $\sigma_{11}|_{x=\pm L_x} = 1, \quad \sigma_{22}|_{y=\pm L_y} = 1, \quad \sigma_{12}|_{x=\pm L_x} = 0, \quad \sigma_{12}|_{y=\pm L_y} = 0.$
  It turns out that the solution to this test problem can be found as the sum of the solutions to Test 1 and Test 2: $\sigma_{ij} = \sigma^1_{ij} + \sigma^2_{ij}$. Therefore, it is possible to use the results already obtained for previous test problems and there is no need to carry out additional numerical calculations. Indeed, the elastic energy for this test problem is calculated using the formula (10). Denoting the solution of the Test 1 as σ^1_{ij} where $\sigma^1_{11} = 1, \sigma^1_{ij} = 0$ if $(ij) \neq (11)$ and solution of the Test 2 as σ^2_{ij} where $\sigma^2_{22} = 1, \sigma^2_{ij} = 0$ if $(ij) \neq (22)$, we calculate strain energies $\mathcal{U}^{01} = \frac{V}{2}s_{1111}$, $\mathcal{U}^{02} = \frac{V}{2}s_{2222}$. This means that compliance moduli s_{1111}, s_{2222} are found and we can compute deformations ε^1_{11}, ε^1_{22}, ε^2_{11},

ε_{22}^2:

$$\begin{aligned}
\varepsilon_{11}^1 &= s_{1111}\sigma_{11}^1 + s_{1122}\sigma_{22}^1 = s_{1111}\sigma_{11}^1 = s_{1111},\\
\varepsilon_{22}^1 &= s_{2211}\sigma_{11}^1 + s_{2222}\sigma_{22}^1 = s_{2211}\sigma_{11}^1 = s_{2211}\\
\varepsilon_{11}^2 &= s_{1122}\sigma_{11}^2 + s_{2222}\sigma_{22}^2 = s_{2222}\sigma_{22}^2 = s_{2222},\\
\varepsilon_{22}^2 &= s_{2211}\sigma_{11}^{02} + s_{2222}\sigma_{22}^2 = s_{2222}\sigma_{22}^2 = s_{2222}.
\end{aligned} \tag{12}$$

Finally, since the solution to this test problem is the sum of the solutions for Test 1 and Test 2, we numerically calculate the energy $\mathcal{U}^0$, which should be equal to

$$\mathcal{U}^0 = \frac{1}{2}\int\limits_V \sigma_{ij}\varepsilon_{ij}dV = \frac{1}{2}\int\limits_V \left(\sigma_{ij}^1 + \sigma_{ij}^2\right)\left(\varepsilon_{ij}^1 + \varepsilon_{ij}^2\right)dV = \tag{13}$$

$$\mathcal{U}^{01} + \mathcal{U}^{02} + \frac{1}{2}\int\limits_V \left(\sigma_{ij}^1\varepsilon_{ij}^2 + \sigma_{ij}^2\varepsilon_{ij}^1\right)dV.$$

Thus, from the above equality we conclude that
$s_{1122} = \frac{1}{2V}\int\limits_V \left(\sigma_{ij}^1\varepsilon_{ij}^2 + \sigma_{ij}^2\varepsilon_{ij}^1\right)dV$, where $\sigma_{ij}^1, \varepsilon_{ij}^1, \sigma_{ij}^2, \varepsilon_{ij}^2$ are solutions of Test 1 and Test 2 already obtained numerically. Thus, it is possible to solve the equilibrium problem in the case of a complex stress state without its direct numerical solution and, therefore, reduce the computation time. However, this requires the use of additional memory to store all stress and strain components for simple stress states.

- Test 4
  $\sigma_{11}|_{x=\pm L_x} = 0, \quad \sigma_{22}|_{y=\pm L_y} = 0, \quad \sigma_{12}|_{x=\pm L_x} = 1, \quad \sigma_{12}|_{y=\pm L_y} = 1.$
  In this test problem, the calculated numerically energy for the equilibrium solution is equal to $\mathcal{U}^0 = \frac{V}{2}\left(2s_{1212}(\sigma_{12})^2\right) = Vs_{1212}$. Thus, s_{1212} is found.
- Test 5
  $\sigma_{11}|_{x=\pm L_x} = 0, \quad \sigma_{22}|_{y=\pm L_y} = 1, \quad \sigma_{12}|_{x=\pm L_x} = 1, \quad \sigma_{12}|_{y=\pm L_y} = 1.$
  Similar to how the solution is found in Test 3, the solution to this problem can be obtained as the sum of the solutions from Tests 2 and 4, and we can find $s_{2212} = \frac{1}{2V}\int\left(\sigma_{ij}^1\varepsilon_{ij}^2 + \sigma_{ij}^2\varepsilon_{ij}^1\right)dV$, where $\sigma_{ij}^1, \varepsilon_{ij}^1, \sigma_{ij}^2, \varepsilon_{ij}^2$ are solutions of the problems Test 2 and Test 4 obtained numerically.
- Test 6
  $\sigma_{11}|_{x=\pm L_x} = 1, \quad \sigma_{22}|_{y=\pm L_y} = 0, \quad \sigma_{12}|_{x=\pm L_x} = 1, \quad \sigma_{12}|_{y=\pm L_y} = 1.$
  Just like in the previous test problem, we can find
  $s_{1112} = \frac{1}{2V}\int\limits_V \left(\sigma_{ij}^1\varepsilon_{ij}^2 + \sigma_{ij}^2\varepsilon_{ij}^1\right)dV$, where $\sigma_{ij}^1, \varepsilon_{ij}^1, \sigma_{ij}^2, \varepsilon_{ij}^2$ are solutions of the problems Test 1 and Test 4 respectively.

4 Numerical Homogenization of Heterogeneous Anisotropic Mixture of Solid/Fluid/Porous Media

Wave processes in a heterogeneous mixture consisting of regions of elastic solid, liquid and porous media can be described by a single HTC system of differential

equations formulated in Sect. 2. In this case, the interfaces between regions of different media are described by jumps in the phase volume concentrations.

The essence of the method is as follows: we select a sample of a heterogeneous material with a given structure and solve a series of six stationary equilibrium problems for this sample with the boundary conditions listed in Sect. 3 and calculate the energy for each problem. Next, assuming heterogeneous sample equivalent to a homogeneous elastic one, we can calculate the corresponding effective compliance modulus of based on the known energy of the heterogeneous sample.

The main issue is how to solve the stationary equilibrium problem for a heterogeneous medium. For the HTC model from Sect. 2, direct solution of the equilibrium equations appears to be a difficult task. We propose to apply the time-marching method for solving the boundary value problem, and as a result of integration for a large value of time we will obtain an approximation to the stationary solution of the HTC equilibrium equations. To speed up the calculations, we introduce artificial velocity relaxation, which ensures zero velocity in a finite time. The resulting PDE's system reads as

$$\rho\frac{\partial u_i}{\partial t}+\frac{\partial p}{\partial x_i}-\frac{\partial \Sigma_{ik}}{\partial x_k}+\theta u_i=0, \tag{14a}$$

$$\frac{\partial w_i}{\partial t}+\left(\frac{1}{\rho_1}-\frac{1}{\rho_2}\right)\frac{\partial p}{\partial x_i}+\theta w_i=0, \tag{14b}$$

$$\frac{\partial p}{\partial t}+K\frac{\partial u_k}{\partial x_k}+\frac{\alpha_1\alpha_2}{\rho}(\rho_2-\rho_1)K\frac{\partial w_k}{\partial x_k}=0, \tag{14c}$$

$$\frac{\partial \Sigma_{ik}}{\partial t}-\mu\left(\left(\frac{\partial u_i}{\partial x_k}+\frac{\partial u_k}{\partial x_i}\right)-\frac{2}{3}\delta_{ik}\left(\frac{\partial u_1}{\partial x_1}+\frac{\partial u_2}{\partial x_2}+\frac{\partial u_3}{\partial x_3}\right)\right)=0, \tag{14d}$$

Obviously, as soon as the velocities u_i and w_i become equal to zero, we obtain a solution to the stationary equilibrium problem. In our calculations we take $\theta = 0.005$, which provides a reasonable rate of velocity relaxation. For the resulting steady-state solution, the energy of the inhomogeneous sample can be calculated and compared with the energy of the equivalent elastic sample. This allows one to find all the effective compliance moduli by solving the problems listed in Sect. 3.

5 Numerical Modeling of Effective Anisotropy of Porous Samples with Different Fracture Geometries

In this section, we present the results of applying a numerical homogenisation technique to study the effective anisotropic properties of fluid-saturated porous samples with various inclusion geometries. The simulations are based on the time-marching method for solving system (14) using the finite-difference method on a staggered grid, as described in [11]. The aim of our analysis is to determine the effect of fracture or inclusion geometry on the effective stiffness tensor and the resulting anisotropy of the medium.

5.1 Generation of Heterogeneous Samples with Controlled Geometry

In order to investigate the influence of fracture geometry on effective elastic properties, we generated a set of two-dimensional samples measuring 500×500 pixels, featuring various crack orientations and spatial distributions. The samples consist of two porous phases:

- **Skeleton**: a porous matrix with parameters $V_p = 3800$ m/s, $V_s = 2200$ m/s, $\rho = 2600$ kg/m^3, and porosity $\phi = 0.05$ (water-saturated);
- **Inclusions**: a softer material with parameters $V_p = 1500$ m/s, $V_s = 600$ m/s, $\rho = 1800$ kg/m^3, and porosity $\phi = 0.20$ (water-saturated).

The pore fluid is water with parameters of $V_p^f = 1500$ m/s, $V_s^f = 0$ m/s and density of $\rho_f = 1040$ kg/m^3.

These parameters were chosen to demonstrate a simplified geological model of a sequence of low-permeability sandstones and clays. The matrix corresponds to cemented sandstone with low porosity, while the inclusions represent softer, clay-rich layers with high porosity. Such combinations are typical of thin-bedded sedimentary formations, where the contrast between the constituent phases determines the effective anisotropic response.

The synthetic samples were generated using a stochastic algorithm. Each sample contains a specified number of inclusions, typically 60–100, with a chosen orientation (0°, 45°, 90°, or random) and a fixed thickness of three pixels. Several geometric characteristics were included in the generation procedure. Roughness controls tortuosity by introducing random deviations from a straight line and was set at 50%. Fracture probability determines the probability of crack segmentation along the inclusion length and was set at 40%. Displacement probability determines the probability of lateral displacements and was also set at 40%. Gap size, which controls the length of discontinuities, was set at 2 pixels. This approach allows for the creation of realistic models of layered and fractured media while maintaining control over the dominant fracture geometry.

Using this algorithm, four geometric configurations were considered, as shown in Fig. 1: vertical bands, diagonal bands at 45° to the horizontal axis, a network of intersecting fractures, and a random fracture system. These configurations represent typical fracturing patterns observed in natural geological formations.

After generation, the actual volume fraction of inclusions was calculated for each model and used in the homogenization procedure. The model with vertical stripes contains 48% inclusions and 52% skeleton, while the other three configurations contain 42% inclusions and 58% skeleton. Using these volume fractions together with the saturated phase densities, the average density of the vertical bands model is 2103 kg/m^3, while the average density of the other three samples is 2155 kg/m^3.

5.2 Calculation of Effective Stiffness Tensor

Using the time-marching method described in Sect. 4, we calculated the effective stiffness tensor for each sample with the geometry shown in Fig. 1. The results are

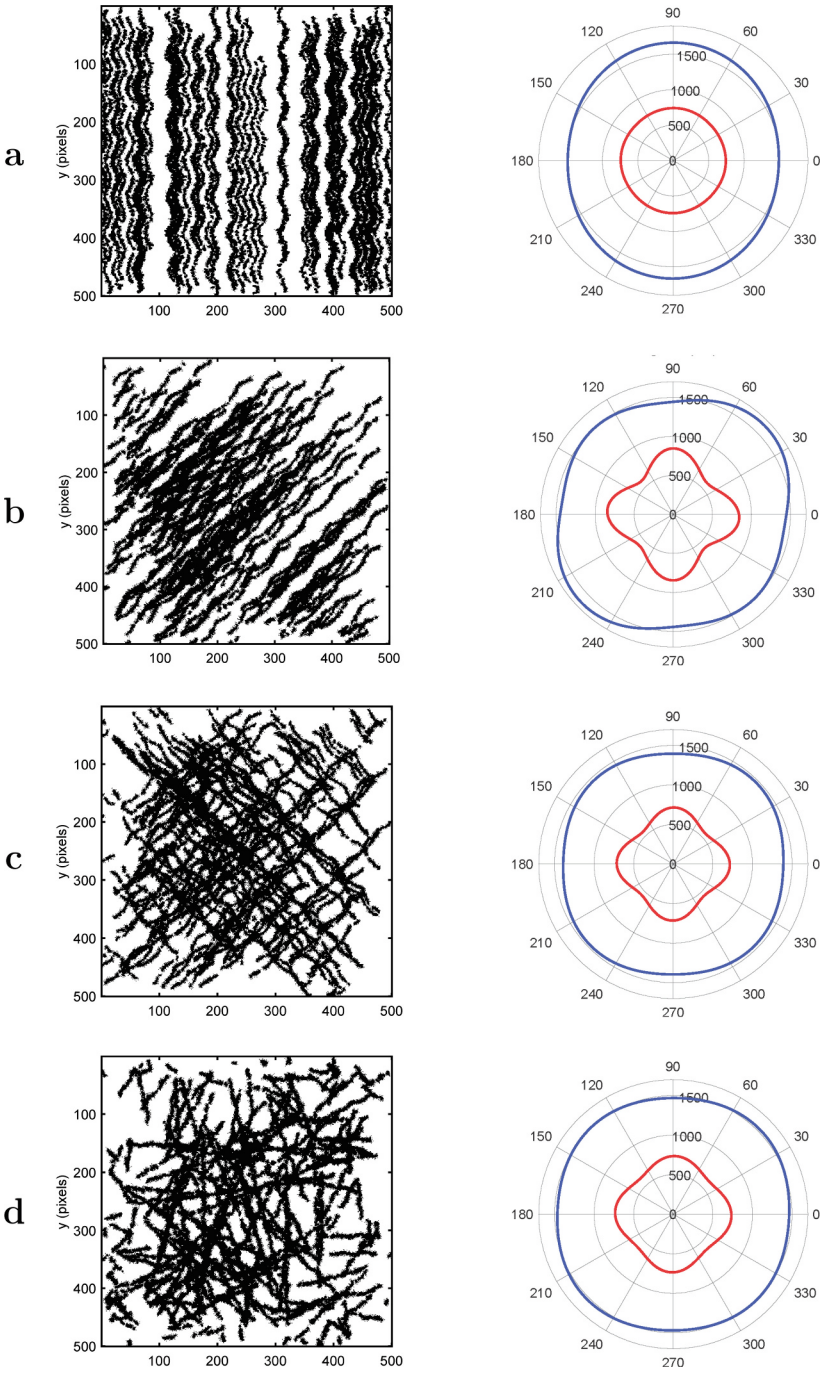

Fig. 1. Synthetic fracture geometries and the corresponding wave-velocity indicatrices: vertical bands (a), diagonal bands at 45° (b), crossed network (c), and random network (d). Blue curves denote V_p, and red curves denote V_s. (Color figure online)

summarized in Table 1, where the stiffness matrix components C_{ij} are given in GPa. In the two-dimensional case, the two-index stiffness matrix C_{ij} is related to the four-index stiffness tensor c_{ijmn} in Hooke's law (6) through the stress–strain relation

$$\begin{pmatrix} \sigma_{11} \\ \sigma_{22} \\ \sigma_{12} \end{pmatrix} = \begin{pmatrix} C_{11} & C_{12} & C_{13} \\ C_{12} & C_{22} & C_{23} \\ C_{13} & C_{23} & C_{33} \end{pmatrix} \begin{pmatrix} \varepsilon_{11} \\ \varepsilon_{22} \\ 2\varepsilon_{12} \end{pmatrix} = \begin{pmatrix} c_{1111} & c_{1122} & c_{1112} \\ c_{1122} & c_{2222} & c_{2212} \\ c_{1112} & c_{2212} & 1212 \end{pmatrix} \begin{pmatrix} \varepsilon_{11} \\ \varepsilon_{22} \\ 2\varepsilon_{12} \end{pmatrix}. \tag{15}$$

Table 1. Comparison of effective stiffness tensor components for different fracture geometries (in GPa).

Component	Vertical	Single	Crossed	Random
C_{11}	4.775	4.488	4.156	4.607
C_{22}	5.958	4.467	4.183	4.637
C_{33}	1.181	1.547	1.097	1.159
C_{12}	3.042	2.972	2.822	2.999
C_{13}	0.023	0.274	0.034	0.057
C_{23}	0.014	0.173	0.013	0.010

6 Analysis of Anisotropy

The anisotropy of the effective medium can be characterised using several parameters derived from the stiffness tensor components. These include the ratios and differences between the in-plane moduli, the coupling coefficients and the directional wave speeds.

6.1 Velocity Indicatrices from the Christoffel Equation

The wave velocities in the fractured samples were obtained by solving the two-dimensional Christoffel equation. The effective wave velocities V^{eff} in an anisotropic medium are determined from

$$\det\left(\Gamma_{ik} - \rho(V^{\text{eff}})^2\delta_{ik}\right) = 0, \tag{16}$$

where $\Gamma_{ik} = c_{ijkl}n_j n_l$ and $\mathbf{n}$ is the propagation direction. This formulation enables the velocities of compressional and shear waves to be computed in each direction and represented as two-dimensional indicatrices. These provide a convenient visualisation of the angular dependence of the wave field. Figure 1 shows the indicatrices for the samples considered. The density ρ in Eq. (16) is the average mixture density of the sample and is calculated as

$$\rho_{avg} = f_{sk}\rho_{sat}^{sk} + f_{inc}\rho_{sat}^{inc}, \tag{17}$$

where f_{sk} and f_{inc} are the volume fractions of skeleton and inclusions, respectively. The saturated phase densities are given by

$$\rho_{sat} = (1 - \phi)\rho_{matrix} + \phi\rho_{fluid}, \tag{18}$$

where ρ_{matrix} is the density of the solid matrix or inclusions, ρ_{fluid} is the pore-fluid density, and ϕ is the porosity. For the considered geometries, the vertical bands model contains 48% inclusions and 52% skeleton, whereas the other three models contain 42% inclusions and 58% skeleton. Using these volume fractions, the average density is found to be $2103\,\mathrm{kg/m^3}$ for the vertical bands model and $2155\,\mathrm{kg/m^3}$ for the remaining configurations.

6.2 Stiffness Anisotropy Parameters

Table 2 summarizes the main anisotropy indicators for the four fracture geometries considered. These quantities are derived from the effective stiffness tensor in Table 1 and provide a compact description of the directionality of the elastic response.

Table 2. Anisotropy parameters for different fracture geometries.

Parameter	Vertical bands	Diagonal (45°)	Crossed network	Random network
C_{11}/C_{22} ratio	0.802	1.005	0.994	0.994
$C_{33}/((C_{11} + C_{22})/2)$	0.219	0.345	0.263	0.252
C_{13} (GPa)	0.023	0.274	0.034	0.057
C_{23} (GPa)	0.014	0.173	0.013	0.010

The C_{11}/C_{22} ratio reflects the degree of in-plane anisotropy. The vertical band configuration exhibits the strongest directional contrast, while the diagonal, cross, and random geometries are much closer to in-plane isotropy. The normalized shear stiffness follows a different trend: it is lowest for vertical bands and highest for diagonal geometries, indicating that oblique cracks redistribute stiffness more strongly toward the shear response.

The off-diagonal coefficients C_{13} and C_{23} quantitatively describe the coupling between normal and shear strains. These terms are small for vertical stripes but increase significantly for a 45° diagonal, confirming strong mode coupling in obliquely cracked media. In cross-fractured and random networks, the coupling remains relatively weak, suggesting that symmetry and statistical averaging reduce the interaction between strain modes.

The effective densities of the samples differ only slightly, so the observed patterns of wave velocity changes are determined primarily by stiffness anisotropy rather than density changes. This means that the angular dependence of velocity indicators primarily reflects the geometry and orientation of the fracture system.

Interpretation of Results. Numerical homogenization shows that the effective elastic response is strongly dependent on the fracture geometry. Vertical bands and bands inclined at 45° are the most anisotropic configurations, while the cross-section and random geometries exhibit a more balanced in-plane response.

The vertical band geometry provides the clearest directionality dependence of the P-wave field. The stiffness tensor exhibits a strong contrast between the principal moduli in the plane, consistent with the vertical orientation of the failure bands. The low normalized shear stiffness and weak coupling coefficients further indicate that the directional contrast in normal stiffness predominates in this configuration.

The single diagonal geometry doesn't simply reduce anisotropy; instead, it rotates and redistributes it. The P-wave indicatrix retains a shape similar to that of vertical stripes, but is rotated by approximately 45°, indicating that the principal axes of anisotropy follow the crack orientation. At the same time, the S-wave indicatrix becomes more dependent on azimuth, reflecting a stronger coupling between normal and shear strain. Thus, diagonal geometry leads to a rotation of P-wave anisotropy and a more pronounced S-wave anisotropy.

The crossing and randomly distributed network structures maintain near-planar isotropy. Stiffness contrasts in them are weak, coupling coefficients are small, and wave velocity indicatrices are more symmetrical than in vertical or diagonally band structures. These results indicate that the crossed and randomly distributed fracture systems redistribute deformation more uniformly and, therefore, suppress strong directional effects.

The differences in density between the samples are small, so the wave velocity behavior is determined primarily by the effective stiffness tensor. In this sense, crack orientation is the dominant factor determining anisotropy, but the P- and S-wave fields respond differently: V_p is more sensitive to the layered structure, while V_s is more sensitive to inclined cracks and mode coupling.

7 Conclusion

This paper presents a numerical approach to estimating the effective elastic properties of heterogeneous porous media saturated with fluid. The method is based on comparing the strain energy of a heterogeneous sample with the strain energy of an equivalent homogeneous elastic medium. Using a thermodynamically consistent hyperbolic model of a two-phase porous medium and additional relaxation terms in the momentum equations, we obtain the effective compliance tensor. The steady-state solutions are computed using a time-marching procedure, providing a stable and convergent numerical algorithm.

The numerical experiments show that the effective elastic response is strongly dependent on crack geometry. The vertical bands and the 45° inclined bands are the most anisotropic configurations, while crossed and random network exhibit a much more balanced in-plane response. The vertical bands exhibit the greatest stiffness contrast between the principal directions, consistent with the vertical orientation of the cracks. Diagonal geometry does not simply reduce anisotropy;

instead, it redistributes it by rotating the principal axes of the P-wave indicatrix and creating more pronounced S-wave anisotropy due to a stronger coupling between normal and shear deformation modes. In contrast, the crossed and random fracture networks remain close to in-plane isotropy, indicating a more uniform strain redistribution.

The density of the samples changes only slightly, so the differences in the wave velocity patterns are mainly influenced by the effective stiffness tensor. Therefore, crack orientation is the primary factor governing anisotropy. However, the sensitivities of P-wave and S-wave propagation differ: P-waves are more affected by layered structures, while S-waves are more sensitive to inclined cracks and the resulting mode interactions.

The proposed approach provides an effective framework for estimating the effective elastic properties of complex heterogeneous materials, explicitly accounting for pore space geometry and the saturating fluid. It is applicable to sedimentary rocks, fractured reservoirs, and composite materials with specified anisotropic properties, and is also relevant for geophysical applications such as seismic interpretation and acoustic logging. Future work will focus on frequency-dependent behaviour, viscoelastic effects, and 3D models with more complex inclusion topologies.

Future work will focus on extending the model to include frequency-dependent behavior and viscoelastic effects, as well as on developing three-dimensional simulations for media with more complex inclusion topology and fracture connectivity.

Acknowledgments. This work was financially supported by the Russian Science Foundation (Project No. 26-11-00165).

Disclosure of Interests. The authors declare that they have no known competing financial interests or personal relationships that could have appeared to influence the work reported in this article.

References

1. Allaire, G., Brizzi, R.: A multiscale finite element method for numerical homogenization. Multiscale Model. Simul. **4**(3), 790–812 (2005)
2. Chen, Z., Xie, Y.M., Wang, Z., Li, Q., Wu, X., Zhou, S.: A comparison of fast fourier transform-based homogenization method to asymptotic homogenization method. Compos. Struct. **238**, 111979 (2020)
3. Gad, A.I., Gao, X.L.: A generalized strain energy-based homogenization method for 2-D and 3-D cellular materials with and without periodicity constraints. Symmetry **13**(10) (2021)
4. Khoei, A.R., Saeedmonir, S., Misaghi Bonabi, A.: Computational homogenization of fully coupled hydro-mechanical analysis of micro-fractured porous media. Comput. Geotech. **154**, 105121 (2023)
5. Otero, F., Oller, S., Martinez, X.: Multiscale computational homogenization: review and proposal of a new enhanced-first-order method. Arch. Comput. Methods Eng. **25**, 479–505 (2018)

6. Otero, F., Oller, S., Martinez, X., Salomon, O.: Numerical homogenization for composite materials analysis. comparison with other micro mechanical formulations. Compos. Struct. **122**, 405–416 (2015)
7. Ponte Castañeda, P.: Variational linear comparison homogenization estimates for the flow of yield stress fluids through porous media. J. Nonnewton. Fluid Mech. **321**, 105104 (2023)
8. Reshetova, G., Romenski, E.: Diffuse interface approach to modeling wavefields in a saturated porous medium. Appl. Math. Comput. **398**, 125978 (2021)
9. Reshetova, G., Romenski, E.: Modeling of temperature-dependent wave fields in deformable porous media saturated with fluid. Numer. Anal. Appl. **17**(4), 358–371 (2024)
10. Reshetova, G., Romenski, E.: Modeling the variability of seismic properties of frozen multiphase media depending on temperature. Sib. Electron. Math. Rep. **21**, B203–B231 (2024)
11. Reshetova, G., Romenski, E.: Numerical implementation of boundary conditions for finite difference method on staggered grid for wave propagation in saturated porous medium. In: Gervasi, O., et al. (eds.) Computational Science and Its Applications - ICCSA 2025 Workshops, pp. 359–375. Springer, Cham (2026)
12. Romenski, E., Reshetova, G., Peshkov, I.: Thermodynamically compatible hyperbolic model of a compressible multiphase flow in a deformable porous medium and its application to wavefields modeling. AIP Conf. Proc. **2448**(1), 020019 (2021)
13. Romenski, E., Reshetova, G., Peshkov, I., Dumbser, M.: Modeling wavefields in saturated elastic porous media based on thermodynamically compatible system theory for two-phase solid-fluid mixtures. Comput. Fluids **206**, 104587 (2020)
14. Saxena, N., Mavko, G.: Estimating elastic moduli of rocks from thin sections: digital rock study of 3D properties from 2D images. Comput. Geosci. **88**, 9–21 (2016)
15. Schneider, M.: A review of nonlinear FFT-based computational homogenization methods. Acta Mech. **232**, 2051–2100 (2021)
16. Tartar, L.: The General Theory of Homogenization: A Personalized Introduction. Lecture Notes of the Unione Matematica Italiana, vol. 7. Springer, Heidelberg (2009)
17. Wei, X., Li, Z., Zhao, G.: A review of multiscale numerical modeling of rock mechanics and rock engineering. Deep Undergr. Sci. Eng. **4**(3), 382–405 (2025)
18. Yesiloglu-Gultekin, N., Dogan, A.: Estimation of the elastic modulus of basaltic rocks using machine learning methods. Earth Sci. Inf. **17**, 5941–5966 (2024)
19. Zhang, W., Dai, G., Wang, F., Sun, S., Bassir, H.: Using strain energy-based prediction of effective elastic properties in topology optimization of material microstructures. Acta. Mech. Sin. **23**, 77–89 (2007)
20. Zochowski, A.: A variational interpretation of homogenization and its extensions. Comput. Struct. **23**(5), 665–669 (1986)